Supplementary Information

Superior High-Temperature Capacitive Energy Storage Performance Enabled by *In Situ* Grown Nanodots in Polymer Nanocomposites

Yanzhi Li,[a] *Yuhan Chen,*[a] *Zhiyuan Li,*[a] *Yuxin Cui,*[a] *Lu Cheng,*[a] *Ke Cao,*[b] *Ying Han,*[c] *Wenfeng Liu,*[a]* *and Yao Zhou*[a]*

[a] State Key Laboratory of Electrical Insulation and Power Equipment, School of Electrical Engineering, Xi'an Jiaotong University, Xi'an, 710049, China

[b] School of Advanced Materials and Nanotechnology, Xidian University, Xi'an 710126, China

[c] Tianjin Key Laboratory of Advanced Joining Technology, School of Materials Science and Engineering, Tianjin University, Tianjin 300350, China

E-mail: liuwenfeng@xjtu.edu.cn, zhouyao@xjtu.edu.cn

Experimental

Materials

4,4′-(4,4′-isopropylidenediphenoxy) diphthalic anhydride (BPADA), 4,4′-diaminodiphenyl sulfone (DDS), tantalum ethoxide ($Ta(OC_2H_5)_5$), and anhydrous *N*-methyl-2-pyrrolidone (NMP, 99.5%) were purchased from Sigma-Aldrich. Ta_2O_5 nanoparticles (Ta_2O_5-NP, ~100 nm) were obtained from Aladdin. Commercial films of BOPP, PI (Kapton), and PEI (Ultem) were supplied by Poly*K* Technology.

Materials synthesis and film preparation

The *in situ* constructed SPEI/TaO nanocomposites were synthesized through three steps: pre-polymerization, co-polymerization, and thermal imidization. In the pre-polymerization step, DDS (124 mg, 0.5 mmol) and BPADA (260 mg, 0.5 mmol) were dissolved in NMP (3.5 mL) and stirred at room temperature for 12 h to form a viscous solution of sulfonated poly(ether amide acid) (SPEAA). For co-polymerization, SPEAA was copolymerized with $Ta(OC_2H_5)_5$ using a site-isolation strategy. $Ta(OC_2H_5)_5$ was dissolved in NMP (7 mL), while the required amount of water was dissolved in an additional 3.5 mL of NMP. The SPEAA/NMP, $Ta(OC_2H_5)_5$/NMP, and water/NMP solutions were mixed and stirred at room temperature for 1 h. The amounts of $Ta(OC_2H_5)_5$ and water were calculated according to:

$$m_{\mathrm{Ta(OC_2H_5)_5}} = \frac{m_{\mathrm{SPEI}}}{\rho_{\mathrm{SPEI}}} \times \frac{V_{\mathrm{Ta_2O_5(vol\%)}} \times \rho_{\mathrm{Ta_2O_5}}}{M_{\mathrm{Ta_2O_5}}} \times 2 \times M_{\mathrm{Ta(OC_2H_5)_5}}$$

$$m_{\mathrm{H_2O}} = \frac{m_{\mathrm{Ta(OC_2H_5)_5}}}{M_{\mathrm{Ta(OC_2H_5)_5}}} \times 5 \times M_{\mathrm{H_2O}}$$

where $\rho_{\mathrm{Ta_2O_5}}$ and ρ_{SPEI} are the densities of Ta_2O_5 (8.20 g cm^{-3}) and SPEI (1.30 g cm^{-3}), respectively; $M_{\mathrm{Ta(OC_2H_5)_5}}$, $M_{\mathrm{Ta_2O_5}}$, and $M_{\mathrm{H_2O}}$ are the molecular weights of $Ta(OC_2H_5)_5$ (406.25 g mol^{-1}), Ta_2O_5 (441.89 g mol^{-1}), and water (18.02 g mol^{-1}), respectively; $m_{\mathrm{Ta(OC_2H_5)_5}}$, m_{SPEI}, and $m_{\mathrm{H_2O}}$ are the weights of $Ta(OC_2H_5)_5$, S-PEI, and water, respectively; and $V_{\mathrm{Ta_2O_5(vol\%)}}$ is the desired volume fraction of Ta_2O_5 in the nanocomposites. In the thermal imidization step, precursor solutions were drop-cast onto pre-cleaned glass slides and dried at 70 °C for 7 h to remove solvent. The films were then heated sequentially at 150 °C for 1 h, 220 °C for 2 h, and 270 °C for 1 h to complete imidization. After cooling, the films were peeled off by soaking in deionized water and subsequently vacuum-dried at 150 °C for 4 h.

For comparison, SPEI/TaO-NP films were fabricated by dispersing commercial Ta_2O_5 nanoparticles into the SPEAA/NMP solution via ultrasonication, followed by the same thermal imidization protocol. Typical films thickness was ~10 μm. Gold electrodes (~60 nm thick) were

sputtered onto both sides of the films using a Quorum Q150R S Plus magneton sputter coater. Electrode diameters were 10 mm for dielectric spectroscopy, and 3 mm for conduction current, electrical breakdown, *D-E* loop, charge–discharge cycling, and fast discharge measurements.

Structural characterization

Fourier transform infrared (FTIR) spectra were collected in attenuated total reflectance (ATR) mode on a Shimadzu IRprestige-21. X-ray photoelectron spectroscopy (XPS) was carried out using a ULVAC-PHI Genesis 500. X-ray fluorescence (XRF) spectra were acquired with a MEGREZ-α spectrometer. Scanning electron microscopy (SEM) was performed on a ZEISS Sigma 360, with cross-sectional samples fractured in liquid nitrogen and coated with ~5 nm of gold. Transmission electron microscopy (TEM) was conducted on a Thermo Fisher Talos F200X. Differential scanning calorimetry (DSC) was measured using a TA Instrument Discovery 250 from 30 °C to 300 °C at 10 °C min^{-1} under nitrogen. Mechanical tests were performed on samples (3 mm × 40 mm) stretched at 2.0 mm min^{-1}, and Young's modulus was obtained from the slope at 0.5% strain.

Electrical characterization

Frequency- and temperature-dependent dielectric spectra were measured using a Keysight 4980AL LCR meter with a Sun Electronics Systems EC1A chamber. Conduction current was recorded using a Keithley 6517A electrometer under controlled electric fields (Stanford PS350) and temperatures (Sun Electronics Systems EC1A chamber). Electrical breakdown strength was measured using a Trek 610C amplifier with a voltage ramp rate of 500 V s^{-1}. Each sample was tested at least 15 times and analyzed using two-parameter Weibull distribution. *D-E* loops were obtained using a modified Sawyer-Tower circuit (PolyK PK-FERRO20B) with a unipolar triangle voltage at 100 Hz. Charging–discharge cycling was performed using the same system in fatigue mode. Fast discharge tests were carried out using a PolyK PK-CPR1502 and a Trek 10/10B high-voltage amplifier, and the charged samples were discharged through a 20 kΩ noninductive resistor via a high-speed MOSFET switch. The discharge time $t_{90\%}$ is defined as the time to release 90% of the stored energy ($U_{90\%}$), and power density is calculated as $U_{90\%}/t_{90\%}$. Thermally stimulated depolarization current (TSDC) was measured using a Keithley 6517A with a Sun Electronics EC1A oven. Samples were polarized at 25 MV m^{-1} and 230 °C for 30 min, rapidly cooled to −50 °C under electric bias. After stabilizing at −50 °C for 3 min, the samples were short-circuited for 1 min. Finally, the samples were heated to 300 °C at 3 °C min^{-1} while recording current. For electrical breakdown, *D-E* loop, and fast discharge tests, samples were immersed in dimethylsiloxane (Dow Corning) with temperature controlled by a hot plate and monitored with a sensor.

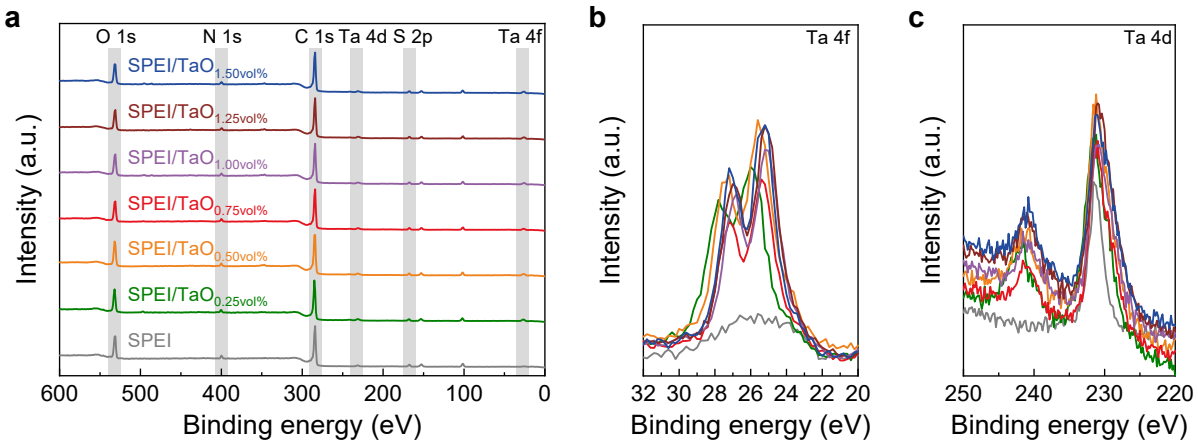

Figure S1. a) XPS survey spectra of SPEI/TaO. b) High-resolution Ta 4f spectra and c) Ta 4d spectra, confirming the successful incorporation of Ta_2O_5 into the nanocomposites.

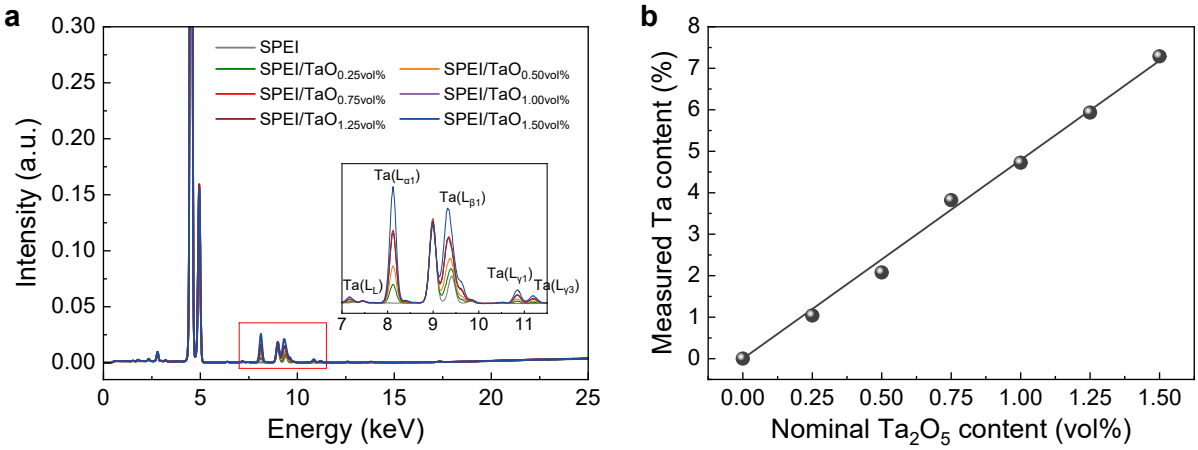

Figure S2. a) XRF spectra of SPEI/TaO. b) Measured Ta content from XRF versus nominal Ta_2O_5 nanodot content. The black line shows the linear fit, demonstrating excellent agreement between the actual and targeted filler loadings.

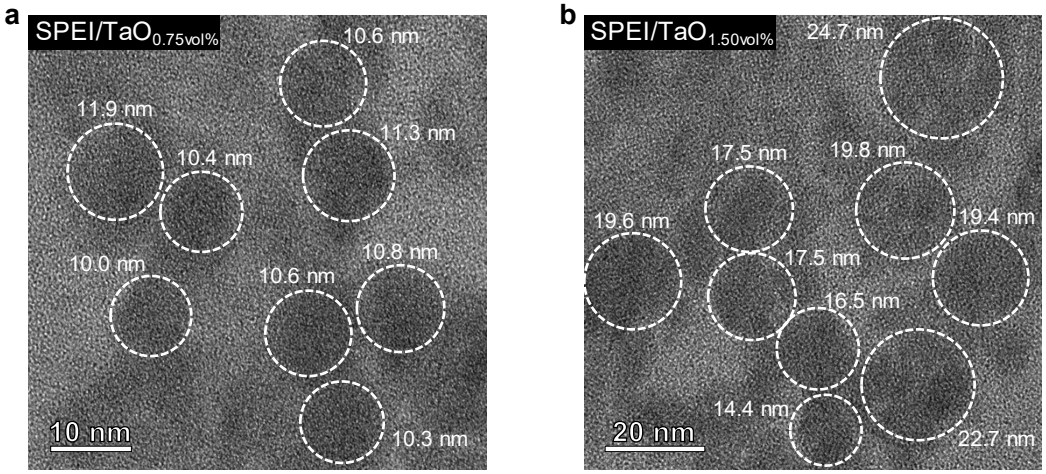

Figure S3. TEM images of SPEI/TaO containing (a) 0.75 vol% and (b) 1.50 vol% Ta_2O_5 nanodots.

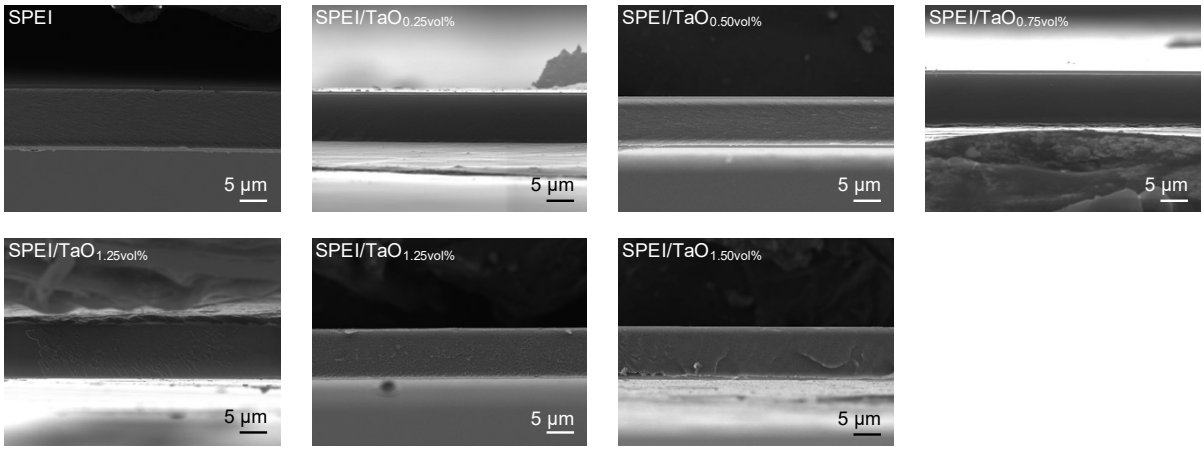

Figure S4. Cross-sectional SEM images of SPEI/TaO, confirming uniform morphology and consistent film thickness.

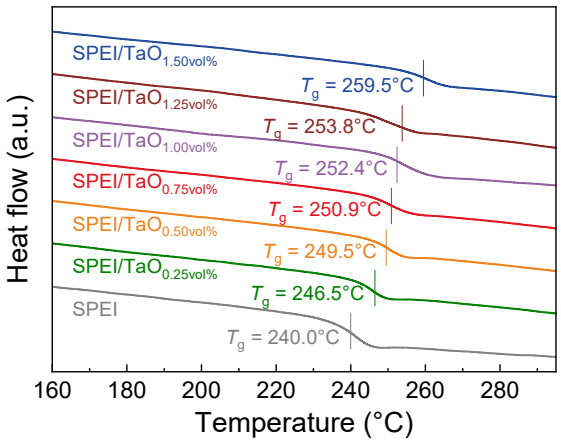

Figure S5. DSC curves of SPEI/TaO, showing an increase in glass transition temperature with increasing Ta_2O_5 nanodot content.

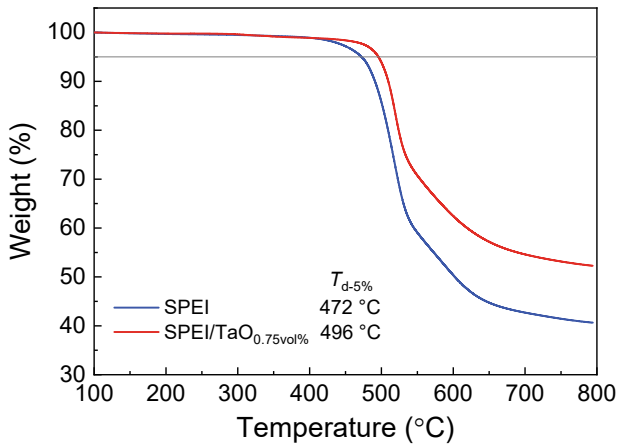

Figure S6. Thermal decomposition temperatures ($T_{d\text{-}5\%}$, defined as the temperature at 5% weight loss) derived from thermogravimetric analysis of SPEI/$TaO_{0.75vol\%}$ and SPEI.

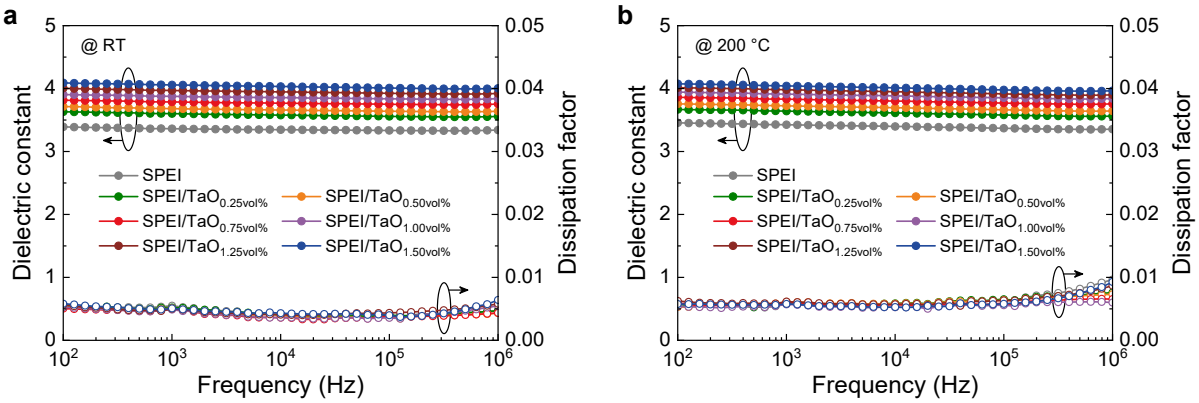

Figure S7. Frequency-dependent dielectric constant and dissipation factor of SPEI/TaO measured at (a) room temperature and (b) 200 °C.

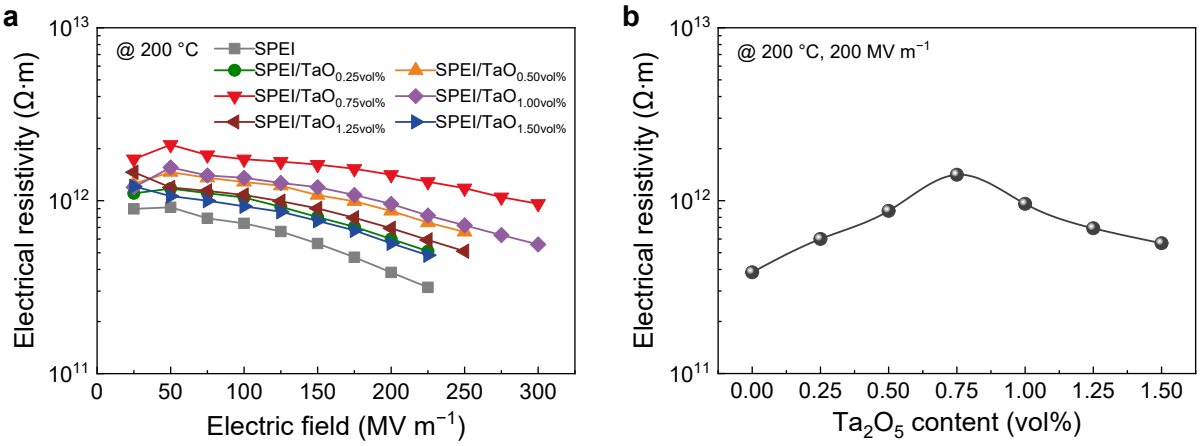

Figure S8. (a) Electric field-dependent resistivity of SPEI/TaO at 200 °C. (b) Electrical resistivity of SPEI/TaO as a function of Ta_2O_5 nanodot content at 200 °C and 200 MV m^{-1}.

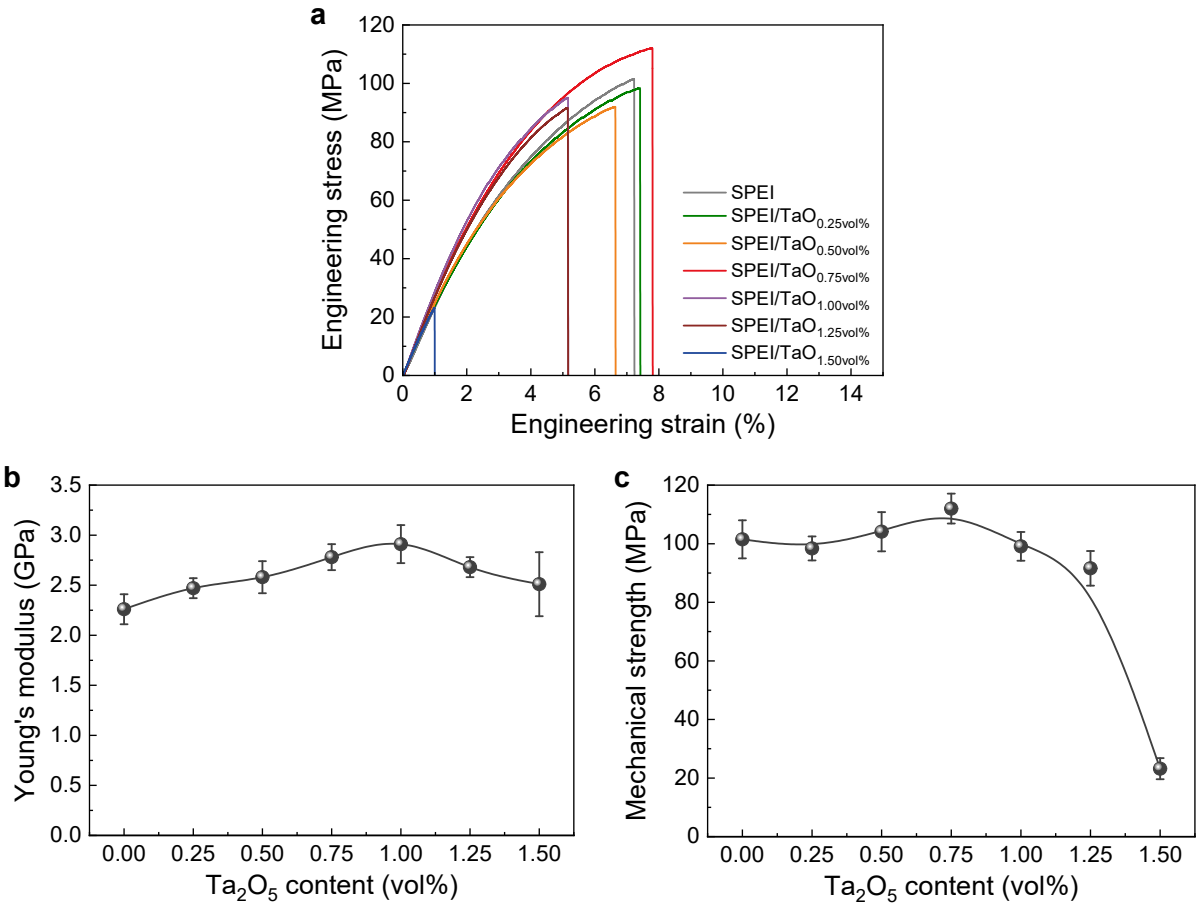

Figure S9. (a) Engineering stress-strain curves of SPEI/TaO. (b) Young's modulus and (c) mechanical strength of SPEI/TaO as a function of Ta_2O_5 nanodot content.

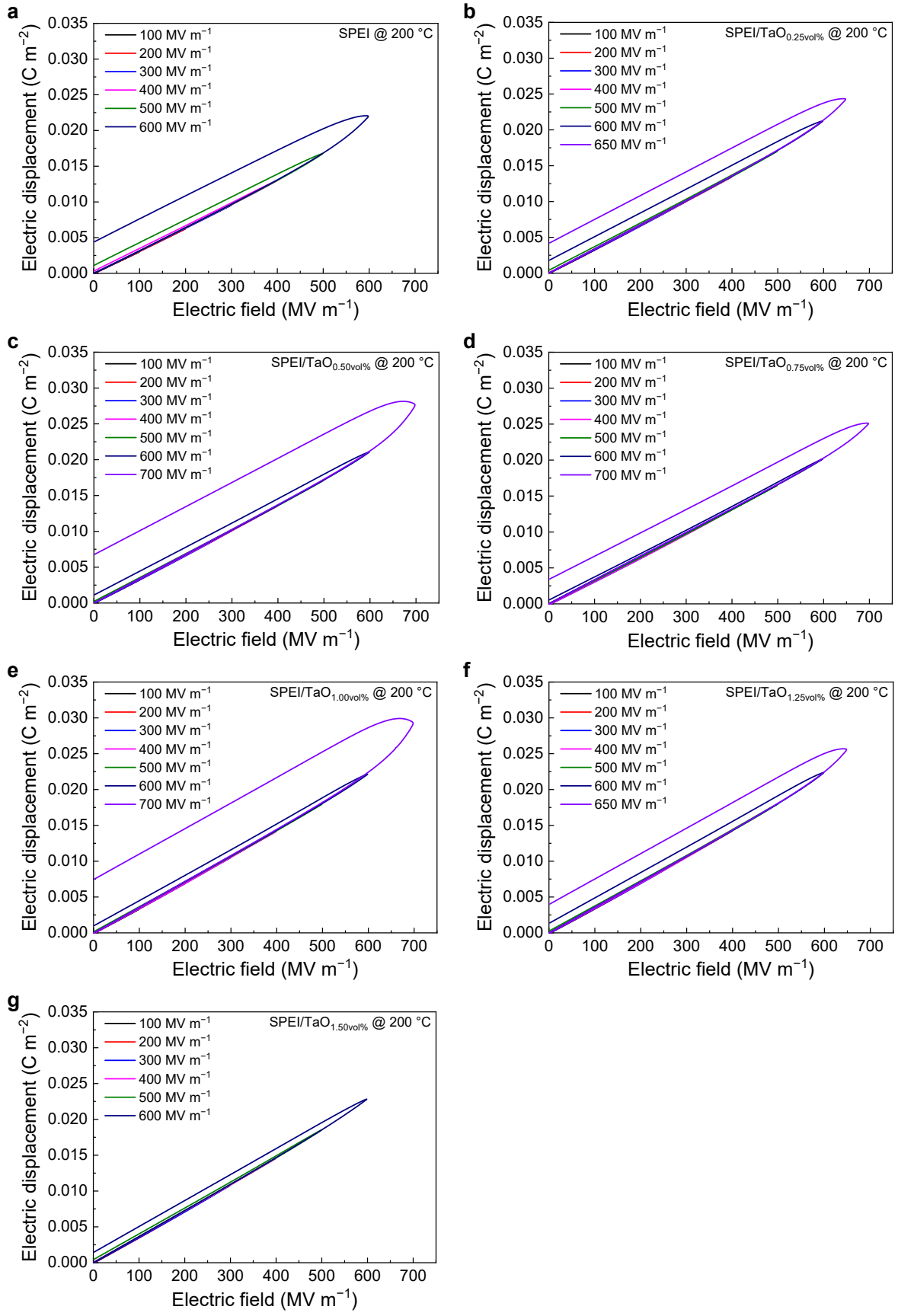

Figure S10. Unipolar *D-E* loops of (a) SPEI, (b) SPEI/$TaO_{0.25vol\%}$, (c) SPEI/$TaO_{0.50vol\%}$, (d) SPEI/$TaO_{0.75vol\%}$, (e) SPEI/$TaO_{1.00vol\%}$, (f) SPEI/$TaO_{1.25vol\%}$, and (g) SPEI/$TaO_{1.50vol\%}$ measured at 200 °C.

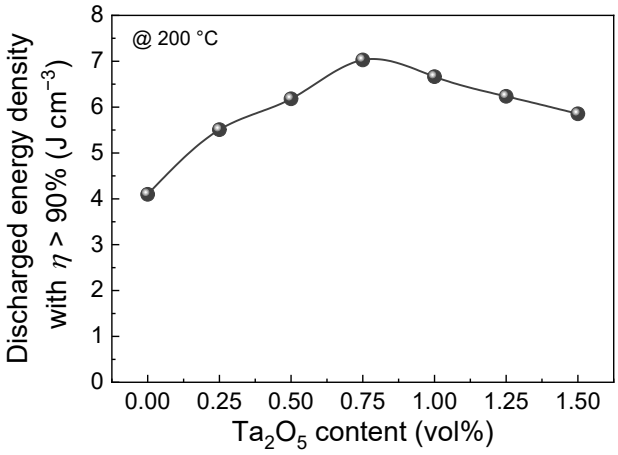

Figure S11. Discharged energy density of SPEI/TaO with efficiency above 90% at 200 °C as a function of Ta_2O_5 nanodot content.

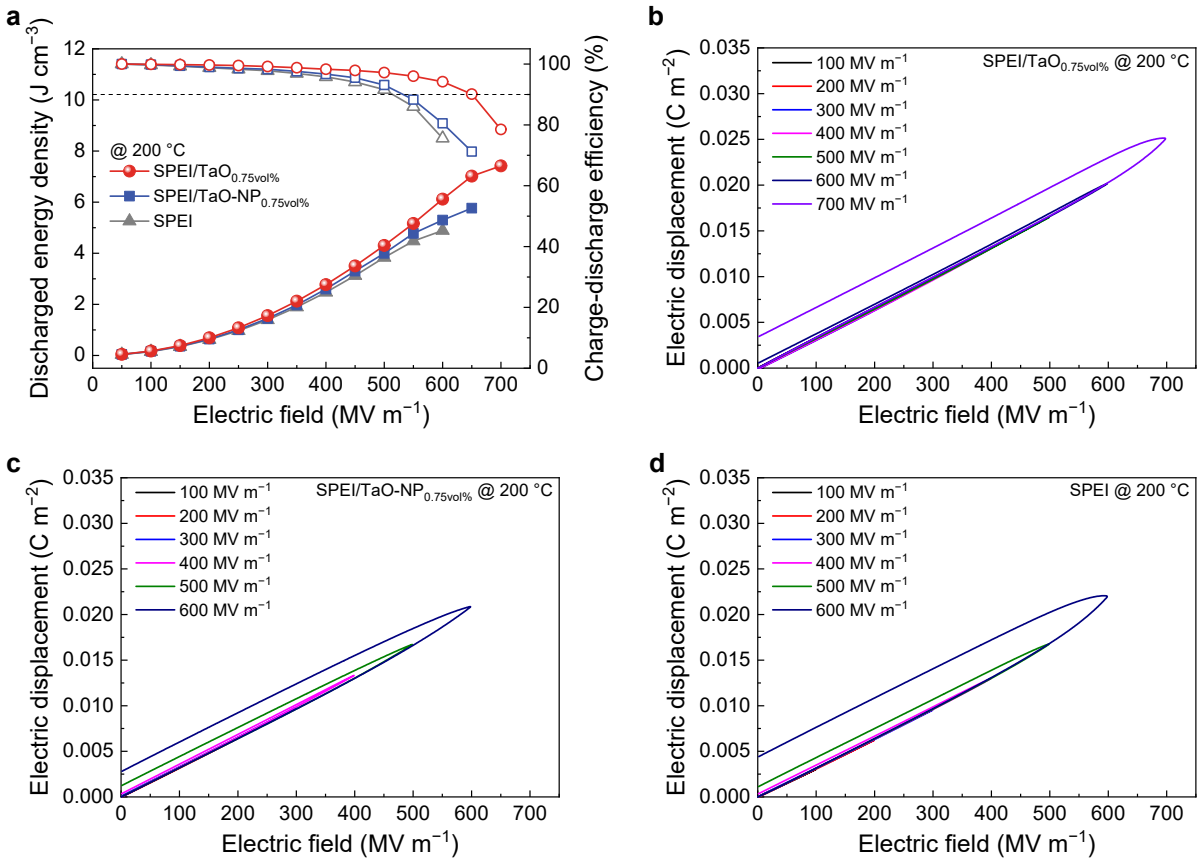

Figure S12. (a) Discharged energy density and charge–discharge efficiency, and the corresponding *D-E* loops of (b) SPEI/$TaO_{0.75vol\%}$, (c) SPEI/TaO-$NP_{0.75vol\%}$, and (d) SPEI measured at 200 °C.

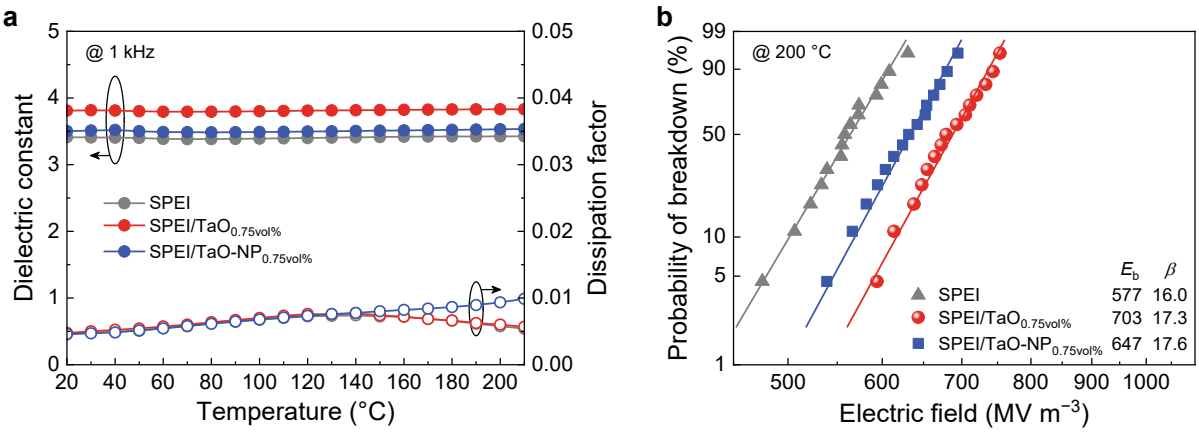

Figure R13. (a) Dielectric constant and dissipation factor, and (b) Weibull breakdown plots of *in situ* constructed SPEI/$TaO_{0.75vol\%}$, directly blended SPEI/TaO-$NP_{0.75vol\%}$, and SPEI measured at 200 °C.

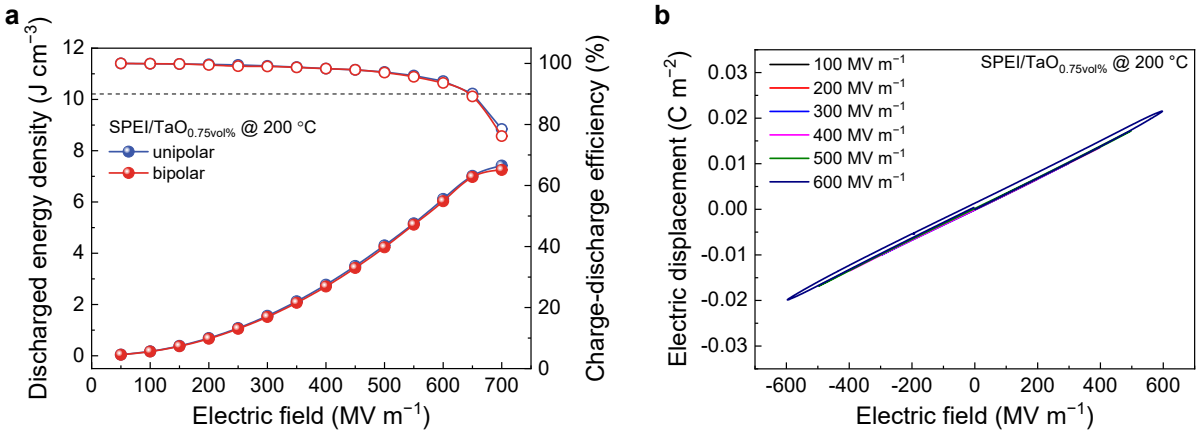

Figure S14. (a) Bipolar *D-E* loops and (b) the corresponding discharged energy density and charge–discharge efficiency of SPEI/$TaO_{0.75vol\%}$ at 200 °C.

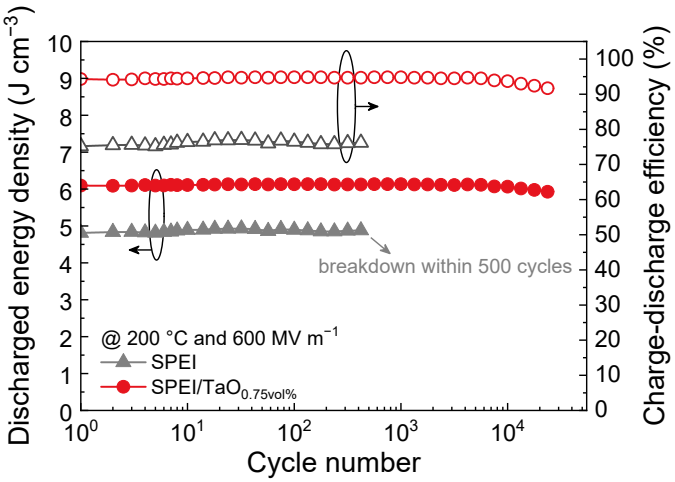

Figure S15. Charge–discharge cycling performance of SPEI and SPEI/TaO$_{0.75vol\%}$ at 200 °C and 600 MV m^{-1}.

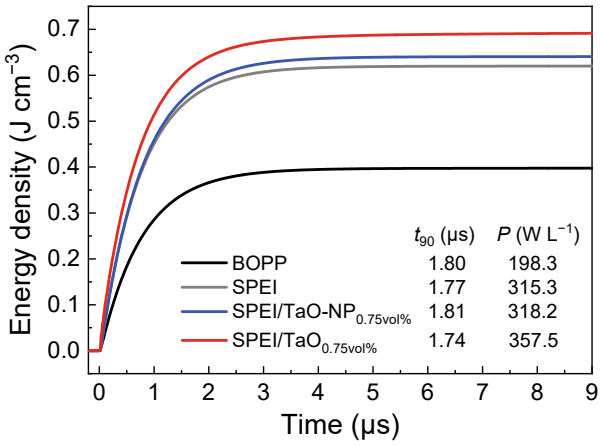

Figure S16. Discharged energy density versus discharge time for BOPP at 105 °C, and for SPEI, directly blended SPEI/TaO-NP$_{0.75vol\%}$, and *in situ* constructed SPEI/TaO$_{0.75vol\%}$ at 200 °C.

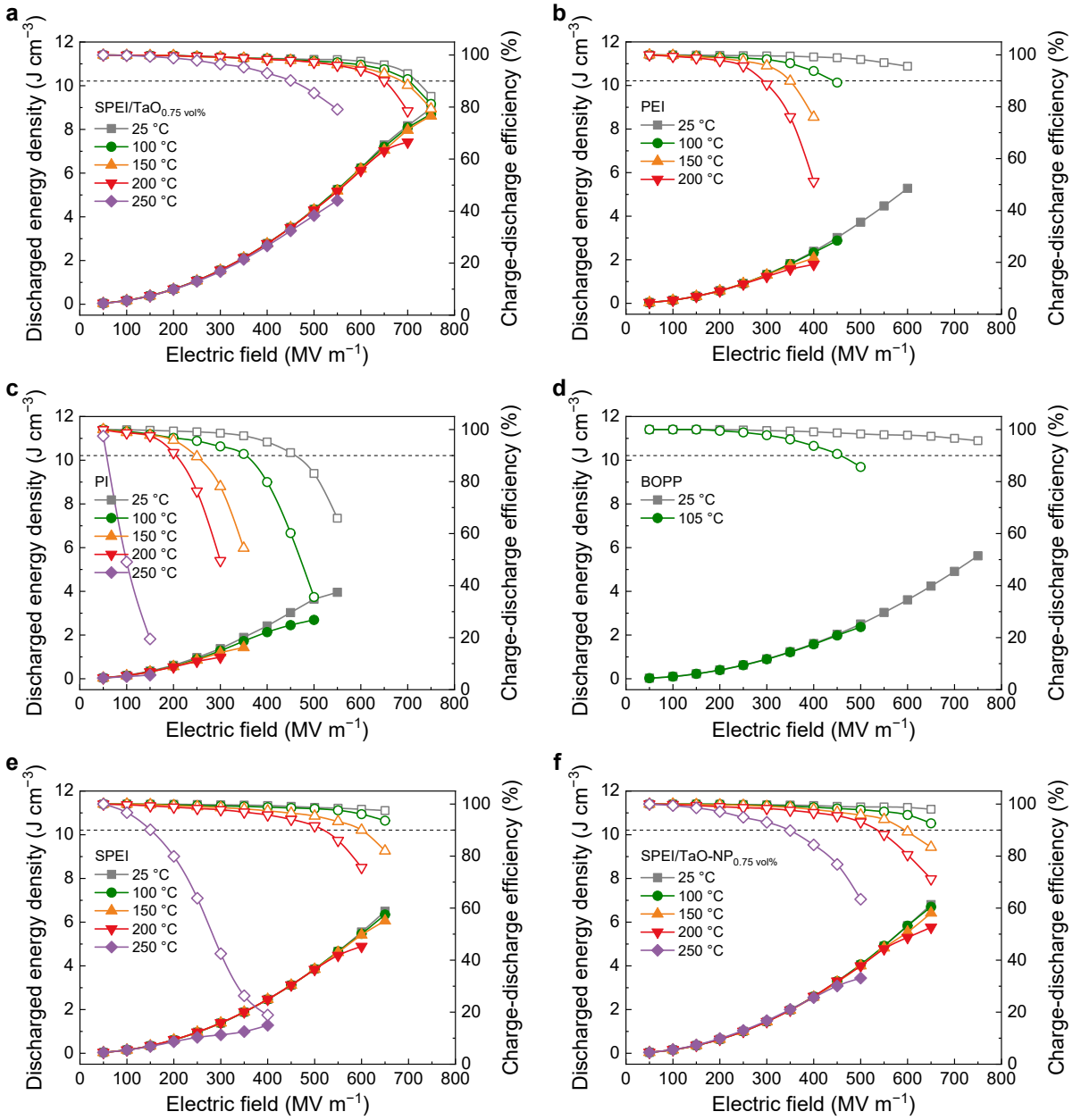

Figure S17. Discharged energy density and charge–discharge efficiency of (a) SPEI/TaO$_{0.75vol\%}$, (b) PEI, (c) PI, (d) BOPP, (e) SPEI, and (f) SPEI/TaO-NP$_{0.75vol\%}$ measured at different temperatures.

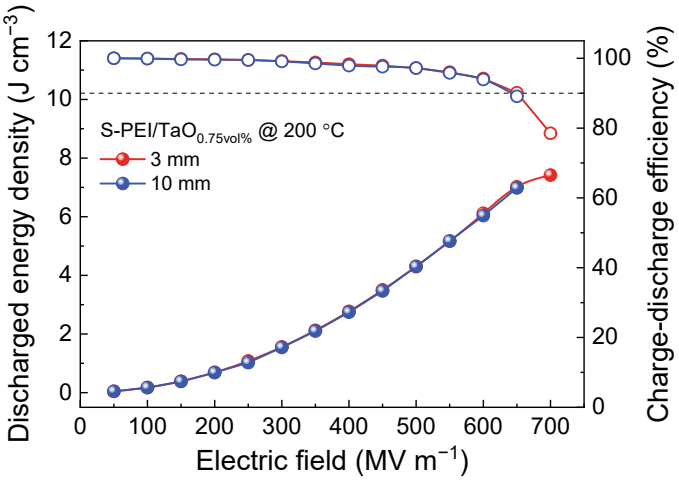

Figure S18. Discharged energy density and charge–discharge efficiency of SPEI/$TaO_{0.75vol\%}$ measured with different electrode areas at 200 °C.

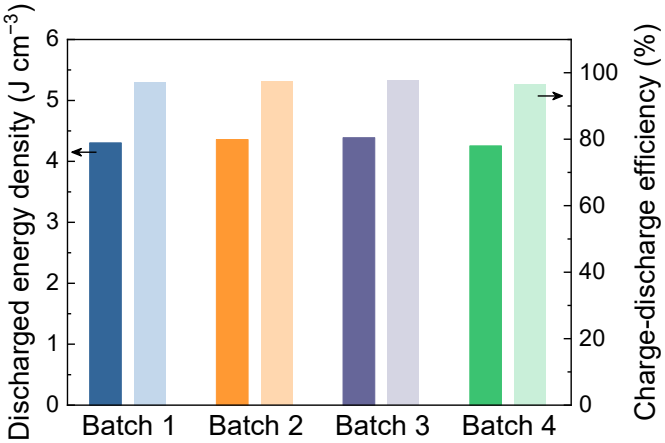

Figure S19. Discharged energy density and charge–discharge efficiency of different batches of SPEI/$TaO_{0.75vol\%}$ measured at 200 °C and 500 MV m^{-1}.

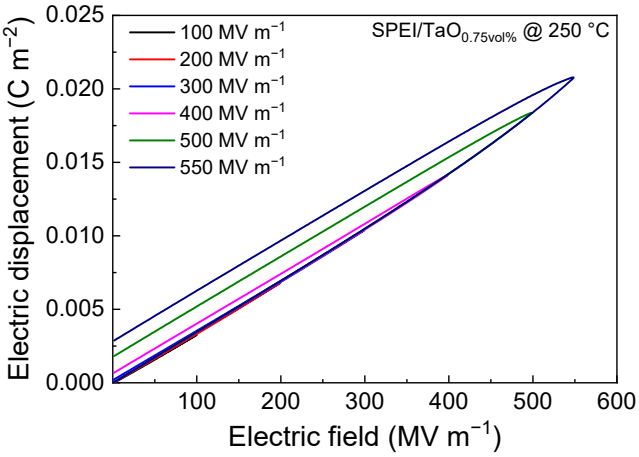

Figure S20. Unipolar *D*-*E* loops of SPEI/$TaO_{0.75vol\%}$ measured at 250 °C.